A Novel Method for Polarization Orientation Angle Estimation Over Steep Terrain and Comparison of Deorientation Algorithms

Liting Liang, *Graduate Student Member, IEEE*, Yunhua Zhang, *Member, IEEE*, and Dong Li, *Member, IEEE*

***Abstract*— This article proposes a novel polarization orientation angle (POA) estimation algorithm for steep terrain by applying physical scattering characteristics of natural surface. The algorithm extends the range of POA from $[-45°, 45°]$ to $(-90°, 90°]$ and achieves consistent estimation with the widely used circular polarization algorithm (CPA) and minimum cross-polarization algorithm (MXPA) over flat area, but avoids the POA wrapping caused by the restriction of CPA and MXPA over precipitous area. Besides, detailed comparison among these deorientation algorithms is presented for clarifying their relations and analyzing the wrapping and unwrapping issue of POA. Both simulated data of Bragg scattering model and PolSAR data of L-band ALOS PALSAR and P-band NASA/JPL AIRSAR are used to substantiate the proposals.**

***Index Terms*— Circular polarization algorithm (CPA), polarimetric synthetic aperture radar (PolSAR), polarization orientation angle (POA), range extension, steep terrain.**

I. Introduction

POLARIMETRIC synthetic aperture radar (PolSAR) system can acquire the fully polarimetric scattering information of target. It has been successfully applied to terrain/land-use classification and target recognition. However, the polarization orientation angle (POA) induced by target rotation about the line of sight (LOS) of radar will change the target scattering characteristics and result in misclassification and misidentification [1], [2]. Deorientation operations have been proposed to estimate POA and compensate its effect on target polarization states [1]–[12]. The current deorientation techniques can be broadly attributed into two categories. One is the circular polarization algorithm (CPA) developed by Lee *et al.* [4]–[6] on the basis of terrain reflection symmetry hypothesis. CPA restricts POA in the range of $[-45°, 45°]$ after removing a bias and shows very consistent POA estimation with the real topography acquired by interferometric SAR system. The other is the minimum cross-polarization algorithm (MXPA), which was first proposed by Xu and Jin with POA ranging from 0° to 180° [7], and An *et al.* then combined deorientation process into model-based decomposition with POA ranging from −90° to 90° (but the POA utilized by An *et al.* for deorientation is restricted into $[-45°, 45°]$ finally [8], [9]). In 2011, Yamaguchi *et al.* [10] developed the four-component model-based decomposition with rotation of coherency matrix by implementing POA compensation before decomposition so as to minimize the cross-polarized (x-pol) component. Moreover, Chen *et al.* [11] extended the range of Yamaguchi POA from $[-22.5°, 22.5°]$ to $[-45°, 45°]$ and investigated the deorientation effects over oriented built-up areas. Even if these algorithms are proposed for different application scenarios, all of them make deorientation an indispensable preprocessing procedure for model-based decomposition and classification [7]–[15].

Nevertheless, there are still two vital issues on POA estimation that need to be addressed. First, since the POA estimated by most algorithms is limited to $[-45°, 45°]$, even if it is physically true in many cases, wrapped estimation will be inevitable over steep terrain. Second, the similarities and differences of different deorientation algorithms need to be clarified so that given PolSAR data can be compensated with the most appropriate algorithm.

In this article, the $E = 0$ deorientation algorithm (EDA) category which includes CPA and MXPA, where E is the Huynen parameter, is analyzed based on the physical scattering properties of Huynen parameters. By further applying the physical constraint of the terrain, a vertical-polarization dominated EDA (VEDA) is proposed to extend the range of POA to $(-90°, 90°]$ and remove the POA wrapping for steep terrain. VEDA can not only achieve the consistent POA estimation with EDA over flat terrain, but also avoid the wrapping caused by the restriction of CPA and MXPA over precipitous area. Experiments on ALOS PALSAR data of Mount Fuji and NASA/JPL AIRSAR data of Chiang Mai validate its nice performance. Besides, detailed comparison among these deorientation algorithms is presented for clarifying their relations and analyzing the wrapping and unwrapping issue of POA.

The remainder of this article is arranged as follows. Section II briefly presents the fundamental theories on deorientation and radar imaging geometry. Based on EDA and the newly introduced physical constraint, VEDA is developed in

Manuscript received July 11, 2019; revised October 31, 2019, February 22, 2020, May 11, 2020, and July 18, 2020; accepted July 27, 2020. Date of publication August 13, 2020; date of current version May 21, 2021. This work was supported in part by the National Natural Science Foundation of China under Grant 41871274 and Grant 61971402 and in part by the Strategic High-Tech Innovation Fund of Chinese Academy of Sciences under Grant CXJJ19B10. *(Corresponding author: Yunhua Zhang.)*

The authors are with the CAS Key Laboratory of Microwave Remote Sensing, National Space Science Center, Chinese Academy of Sciences, Beijing 100190, China, and also with the School of Electronic, Electrical, and Communication Engineering, University of Chinese Academy of Sciences, Beijing 100049, China (e-mail: liangliting16@mails.ucas.ac.cn; zhangyunhua@mirslab.cn; lidong@mirslab.cn).

Color versions of one or more of the figures in this article are available online at https://ieeexplore.ieee.org.

Digital Object Identifier 10.1109/TGRS.2020.3013203

Section III. Section IV compares VEDA with CPA and MXPA in detail, which is substantiated on both simulated data of Bragg scattering model and PolSAR data of L-band ALOS PALSAR and P-band NASA/JPL AIRSAR in Section V. The article is concluded in Section VI.

II. Deorientation and Range of Angles in Radar Imaging Geometry

A. Deorientation Theory

The fully polarimetric scattering of a pure/single target can be modeled by the scattering matrix

$$[S] = \begin{bmatrix} S_{HH} & S_{HV} \\ S_{VH} & S_{VV} \end{bmatrix}. \tag{1}$$

Under the reciprocity condition, we have $S_{HV} = S_{VH}$, and the Pauli vector $\boldsymbol{k}$ is obtained as

$$\boldsymbol{k} = \frac{1}{\sqrt{2}} \begin{bmatrix} S_{HH} + S_{VV} \\ S_{HH} - S_{VV} \\ 2S_{HV} \end{bmatrix}. \tag{2}$$

The target coherency matrix is then expressed as [1], [2]

$$[T] = \langle \boldsymbol{k} \cdot \boldsymbol{k}^{\dagger} \rangle = \begin{bmatrix} T_{11} & T_{12} & T_{13} \\ T_{21} & T_{22} & T_{23} \\ T_{31} & T_{32} & T_{33} \end{bmatrix} = \begin{bmatrix} 2A_0 & C - jD & H + jG \\ C + jD & B_0 + B & E + jF \\ H - jG & E - jF & B_0 - B \end{bmatrix} \tag{3}$$

where superscript † denotes the operation of complex conjugation and transposition, $\langle \cdot \rangle$ denotes ensemble average, T_{ij} is the (i, j) entry of $[T]$, and A_0, B_0, B, C, D, E, F, G, and H are the Huynen parameters [1].

The deorientation of scattering matrix $[S]$ is conducted by [1]

$$[\tilde{S}] = \begin{bmatrix} \cos\varphi & \sin\varphi \\ -\sin\varphi & \cos\varphi \end{bmatrix} [S] \begin{bmatrix} \cos\varphi & -\sin\varphi \\ \sin\varphi & \cos\varphi \end{bmatrix} \tag{4}$$

where φ is the POA of target, $[\tilde{S}]$ and $[S]$ are scattering matrix with and without deorientation, respectively.[1]

The deorientation of coherency matrix $[T]$ is done by

$$[\tilde{T}] = [R_\varphi][T][R_\varphi]^{\dagger} \tag{5}$$

where $[R_\varphi]$ is the SU(3) rotation matrix

$$[R_\varphi] = \begin{bmatrix} 1 & 0 & 0 \\ 0 & \cos 2\varphi & \sin 2\varphi \\ 0 & -\sin 2\varphi & \cos 2\varphi \end{bmatrix}. \tag{6}$$

B. Imaging Geometry and POA Range

Lee *et al.* [4] indicated that the POA of terrain surface is geometrically related to the topographical slopes and radar look angle, following

$$\tan\varphi = \frac{\tan\omega}{-\tan\gamma\cos\phi + \sin\phi} \tag{7}$$

where φ is the POA of the ground patch, ω is the azimuth slope angle, γ is the ground range slope angle, and ϕ is the radar look angle. Fig. 1 shows the radar imaging geometry.

[1]Hereinafter, we represent the deoriented parameter with a superscript $\sim$ for convenience.

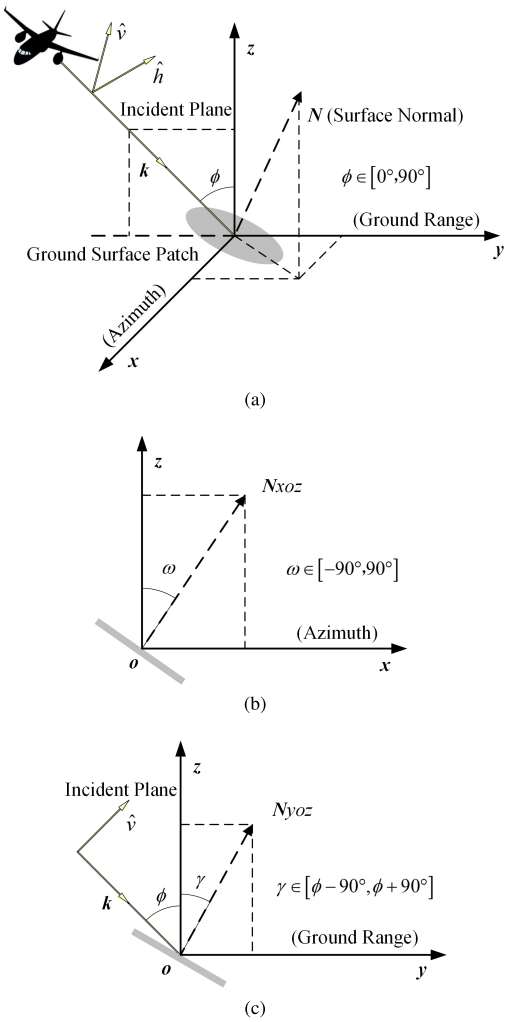

Fig. 1. Radar imaging geometry of a tilted ground surface patch. (a) 3-D view, and the projected view of (b) xoz-plane and (c) yoz-plane, where $\boldsymbol{N}xoz$ and $\boldsymbol{N}yoz$ are projected components of surface normal on xoz-plane and yoz-plane, respectively.

The range of POA can be theoretically derived from (7) when ranges of other angles are given. There is no doubt that radar look angle ϕ varies within $[0°, 90°]$ (see Fig. 1(a)), and azimuth angle ω is limited in $[-90°, 90°]$ (see Fig. 1(b)). As shown in Fig. 1(c), the detectable range of ground range angle γ is $[\phi - 90°, \phi + 90°]$, which depends on ϕ. Here, the negative value of ω and γ means clockwise direction in the corresponding planes xoz and yoz, as shown in Fig. 1(b) and (c). Fig. 2 shows that φ changes as a function of ω and γ, where we set $\phi = 30°$ without loss of generality. It is shown that φ ranges within $[-90°, 90°]$, consistent with the physical reality of steep terrain observed by Lee *et al.* [16]. The function is nonlinear because POA is determined by both ω and γ, while ω plays a major role seemingly.

III. Unambiguous POA Estimation for Steep Terrain

A. Ambiguous Estimation of EDA

CPA and MXPA can be collectively called EDA, because both of them regard $E = 0$ as the necessary condition of terrain zero-POA state [6], which will be discussed in detail later. This reasonable constraint can also be interpreted

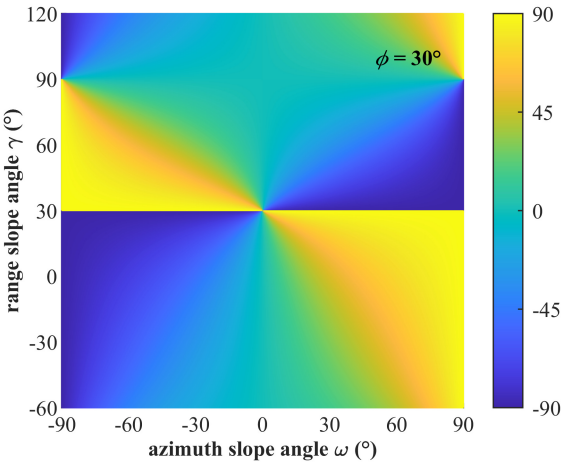

Fig. 2. POA variation as a function of topographic azimuth slope angle ω and ground range slope angle γ with the radar look angle $\phi = 30°$. The POA ranges within $[-90°, 90°]$.

based on the physical scattering properties of Huynen parameters, taking the three prevalent models of terrain surface scattering into account, i.e., Bragg scattering [17], extended Bragg scattering [18], and scattering of reflection symmetry [19]. Even though all of them hold the common property that E, F, G, and H are all zero when with zero-POA rotation, however, as described in [6], only one parameter can be adjusted to zero by rotation mathematically. Compared with parameters G and H, the physical significances of E and F are more relevant to target asymmetry [20], [21], which should be minimized when terrain is flat. Moreover, since F is roll-invariant [6] and represents the helix power [10], the least but optimal choice is to tune parameter E.

Accordingly, EDA can be expressed as

$$\begin{aligned} &\textbf{find} \quad \varphi \\ &\textbf{s.t.} \quad \tilde{E} = 0 \end{aligned} \tag{8}$$

where the deoriented Huynen parameter $\tilde{E}$ can be derived from (3) and (5) as

$$\tilde{E} = -B \sin 4\varphi + E \cos 4\varphi. \tag{9}$$

Since the range of φ is $[-90°, 90°]$, as shown in Fig. 2, two φ values with 90° difference can both satisfy (8), which makes POA not unique. To overcome this, POA estimations such as CPA, restrict φ in $[-45°, 45°]$ (it will be detailed in Section IV that POA derived by (8) in $[-45°, 45°]$ is consistent with that obtained by CPA of Lee *et al.* [4]). Such restrictions, however, will deeply influence the application of EDA to steep terrain slope estimation because wrapping will arise when actual POA exceeds the interval $[-45°, 45°]$. As shown in Fig. 3(a), beyond the interval $[-45°, 45°]$, the CPA-estimated POA φ_L in solid red line is inconformity with the real value derived from DEM in blue broken line. The target is modeled by Bragg scattering, which has the same condition as [16].

B. Unambiguous Estimation of VEDA

The ambiguous problem of POA estimation over steep terrain can be solved felicitously by combining the physical scattering characteristics. As for the natural terrain dominated by Bragg scattering, when POA is zero, the vertical-polarization (v-pol) power $|S_{VV}|^2$ is not less than the horizontal-polarization (h-pol) power $|S_{HH}|^2$ [17]. This indicates a significant fact that deorientation should not only make $E = 0$ but also restrict $C \leq 0$, where $C = \left(|S_{HH}|^2 - |S_{VV}|^2\right)/2$. Therefore, (8) becomes

$$\begin{aligned} &\textbf{find} \quad \varphi \\ &\textbf{s.t.} \quad \begin{cases} \tilde{E} = 0 \\ \tilde{C} \leq 0 \end{cases} \end{aligned} \tag{10}$$

where the deoriented Huynen parameter $\tilde{C}$ can be derived from (3) and (5) as

$$\tilde{C} = C \cos 2\varphi + H \sin 2\varphi. \tag{11}$$

According to (3) and (5), deorientation by the two different POA solutions of (8) affects the sign of $\tilde{C}$ (see Appendix A). Hence, φ is unique when fixing the sign of $\tilde{C}$ and can be succinctly expressed as

$$\begin{cases} \sin(4\varphi + 360° \cdot n) = \dfrac{E}{\sqrt{E^2 + B^2}} \\ \cos(4\varphi + 360° \cdot n) = \dfrac{B}{\sqrt{E^2 + B^2}} \end{cases} \quad n = -1, 0, 1 \tag{12}$$

where $\varphi \in (-90°, 90°]$ (the half open interval is determined by the periodicity of the trigonometric function), and the value of n depends on the sign of $\tilde{C}$ and the range of POA. Note that $\tilde{C}$ is calculated by (11) with $(4\varphi + 360° \cdot n)$, which equals the solution of EDA in $[-45°, 45°]$, e.g., φ_L derived by Lee *et al.* [4]–[6] (proved later in Section IV-A). Accordingly, if $\tilde{C} \leq 0$, then $\varphi = \varphi_L$ (viz., $n = 0$); if $\tilde{C} > 0$ and $-45° \leq \varphi_L \leq 0°$, then $\varphi = \varphi_L + 90°$ (viz., $n = -1$); if $\tilde{C} > 0$ and $0° < \varphi_L \leq 45°$, then $\varphi = \varphi_L - 90°$ (viz., $n = 1$).

Specifically, $\tilde{C} \leq 0$ means that the derived POA satisfies the assumption of Bragg scattering and needs no correction, thus $n = 0$ and the solution is just the same as EDA-derived. When $\tilde{C} > 0$, POA should be corrected, and there are two different cases thus deriving two different values of n. This is because POA after correction should be limited in its effective range, i.e., $(-90°, 90°]$, to be consistent with the range of terrain POA. Therefore, the sign of POA in $[-45°, 45°]$ further determines the sign of n. For convenience, the proposed POA estimation (10) is termed as VEDA. Fig. 3(b) shows POA obtained by VEDA. The result overlaps the DEM-derived POA without wrapping, which substantiates the proposed algorithm perfectly.

IV. Comparison of VEDA and Others

Similarities and differences among VEDA, CPA, and MXPA are discussed in detail in this section from multiple perspectives, which is substantiated by the simulated data.

A. CPA

1) CPA Proposed by Lee et al.: CPA was developed for medium of reflection symmetry [4], which takes advantage of the circular polarization parameter $S_{RR}S_{LL}^*$ based on the hypothesis that

$$\mathrm{Im}\{\tilde{S}_{RR}\tilde{S}_{LL}^*\} = 0 \tag{13}$$

where

$$\begin{cases} \tilde{S}_{RR} = S_{RR}e^{-j2\varphi} \\ \tilde{S}_{LL} = S_{LL}e^{j2\varphi} \end{cases} \tag{14}$$

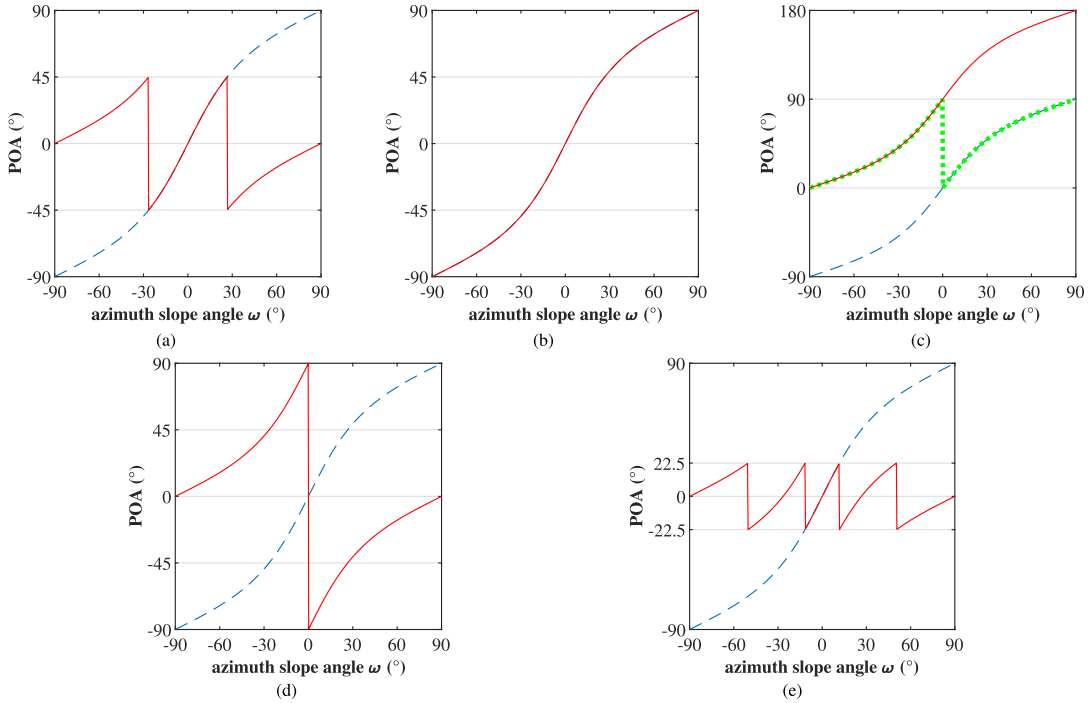

Fig. 3. POA versus azimuth slope angle plots. The blue broken line in each plot denotes the DEM-derived POA φ_{DEM}. The solid red line denotes (a) CPA-derived POA φ_L developed by Lee *et al.* [4], (b) VEDA-derived POA φ, (c) MXPA-derived compensated POA φ_{XJ} by Xu and Jin [7], (d) MXPA-derived compensated POA φ_A by An [9], and (e) MXPA-derived POA φ_Y by Yamaguchi *et al.* [10], respectively. The green dotted line in (c) plots MXPA-derived POA φ_m by Xu and Jin without compensation [7]. Terrain surface is modeled by Bragg scattering with $\varepsilon_r = 9 + j2.5$, ω varies from $-90°$ to $90°$, $\gamma = 0°$, and $\phi = 30°$ [16].

Then, the expression of POA proposed by Lee *et al.* is [5], [6]

$$\varphi_L = \begin{cases} \eta, & \eta \le 45° \\ \eta - 90°, & \eta > 45° \end{cases} \tag{15}$$

where

$$\eta = \frac{1}{4}\left[\tan^{-1}\frac{-E}{-B} + 180°\right]. \tag{16}$$

2) Alternative Solution of CPA: The solution above is not strict, and it is interesting to note that there exists another expression from the hypothesis of reflection symmetry. According to (13) and (14), we have

$$\mathrm{Arg}\{S_{RR}S_{LL}^*\} = \begin{cases} 4\varphi \\ 4\varphi + 180° \end{cases} \tag{17}$$

where Arg{·} denotes the extraction of phase term. Obviously, POA in (15) is derived from the first equation of (17), i.e., $\mathrm{Arg}\{S_{RR}S_{LL}^*\} = 4\varphi$, while the second equation will lead to an alternative solution undoubtedly because it also satisfies the constraint (13). We use α to represent the new POA, and[2]

$$\begin{cases} \sin 4\alpha = \dfrac{E}{\sqrt{E^2+B^2}} \\ \cos 4\alpha = \dfrac{B}{\sqrt{E^2+B^2}} \end{cases}, \quad \alpha \in \left[-45°, 45°\right] \tag{18}$$

where $\alpha = \varphi_L$ (see Appendix B). Therefore, we can directly use (18) to perform CPA, which is more succinct than (15).

According to (18), CPA belongs to EDA category, and as aforementioned, its estimation of POA will be wrapped over the steep terrain when the real orientation exceeds $[-45°, 45°]$ for no dominated co-pol power is specified.

[2]It should be stressed that (18) cannot be expressed as $\alpha = (1/4)\tan^{-1}(E/B)$, otherwise α will be restricted within $[-22.5°, 22.5°]$ instead of $[-45°, 45°]$ in (18). The expression of POA like (18) will be used hereinafter to avoid ambiguity.

B. MXPA

1) MXPA of Xu-Jin and An et al.: Xu and Jin [7] proposed a deorientation algorithm by minimizing the x-pol scattering power of target. They indicated that concentrating power onto the co-pol backscattering can make the corresponding parameters more effective in describing target characteristics. They proved that the MXPA-derived POA φ_m is in agreement with the CPA-derived POA α [7]. However, technically their relation is

$$\varphi_m = \begin{cases} \alpha, & \alpha \ge 0 \\ \alpha + 90°, & \alpha < 0 \end{cases} \tag{19}$$

and the range value of φ_m is $[0°, 90°)$. Furthermore, Xu and Jin indicated that deorientation with φ_m will turn a target into two orthogonal states and φ_m should be corrected by

$$\varphi_{XJ} = \begin{cases} \varphi_m, & \tilde{C} \ge 0 \\ \varphi_m + 90°, & \tilde{C} < 0 \end{cases} \tag{20}$$

Thus, the range of Xu-Jin POA is extended to $[0°, 180°)$.

An *et al.* [8] estimated POA for model-based decomposition by minimizing $\tilde{T}_{33}$ which bears the same form as α. Similarly, An further corrected POA by judging the predominated polarization in his dissertation [9], and the An POA φ_A can be finally expressed by α as

$$\varphi_A = \begin{cases} \alpha, & \tilde{C} \ge 0 \\ \alpha + 90°, & \tilde{C} < 0 \text{ and } \alpha \le 0 \\ \alpha - 90°, & \tilde{C} < 0 \text{ and } \alpha > 0. \end{cases} \tag{21}$$

The range of φ_A is $(-90°, 90°]$ [9].

Essentially, the algorithms developed by Xu-Jin [7] and An [9] are the same, i.e., minimizing the x-pol power and correcting the result based on the sign of $\tilde{C}$. However, the ranges of

φ_{XJ} and φ_A are different because of their different rotation directions. φ_{XJ} in (20) is always positive which indicates the same rotation direction, while φ_A in (21) is symmetric around 0°, which indicates two different rotation directions.

2) MXPA of Yamaguchi and Chen et al.: In 2011, Yamaguchi *et al.* [10] indicated that the x-pol component can also be created by multiple scattering in man-made structures with oblique incidence angle which will confuse the recognition of urban area. Hence, the deorientation process is required so as to minimize the x-pol component $\tilde{T}_{33}$ like Xu-Jin [7] and An *et al.* [8], [9]. The Yamaguchi POA φ_Y is obtained from derivation

$$\tilde{T}'_{33} = 2(T_{22} - T_{33})\sin 4\varphi - 4\mathrm{Re}\{T_{23}\}\cos 4\varphi = 0 \quad (22)$$

and formulated as

$$\tan 4\varphi_Y = \frac{E}{B}. \quad (23)$$

It should be noted that (23) is derived only by (22), which specifies $\tan 4\varphi_Y$ with no information on the sign of $\sin 4\varphi_Y$ and $\cos 4\varphi_Y$. Therefore, even if it seems equivalent to (18), the main range of φ_Y is limited in $[-22.5°, 22.5°]$.

Besides, only the first derivative condition cannot guarantee that $\tilde{T}_{33}$ will be minimized by rotation. Accordingly, Chen *et al.* [11] introduced the second derivation condition when they estimated POA for built-up areas

$$\tilde{T}''_{33} = 8(T_{22} - T_{33})\cos 4\varphi + 16\mathrm{Re}\{T_{23}\}\sin 4\varphi > 0. \quad (24)$$

The Chen POA φ_C is then expressed as [11]

$$\varphi_C = \frac{1}{4}\left(\tan^{-1}\frac{E}{B} \pm n\pi\right), \quad n = 0, 1. \quad (25)$$

The range of φ_C is $[-45°, 45°]$. In Appendix C, we prove that φ_C is equivalent to the CPA POA α.

3) Remarks: As shown in (20), (21), (23), and (C.5), φ_{XJ}, φ_A, φ_Y, and φ_C obtained by MXPA are directly related to α in (18) achieved by CPA despite the differences on range. Like CPA, MXPA also supports POA is 0 when $E = 0$, because the minimizing of x-pol entry is, in fact, equivalent to the maximizing of $\tilde{B}$, which further requires $\tilde{E}^2$ to be minimized by rotation, i.e., rotation is not needed if $E = 0$, as can be simply derived from (3) and (5). Therefore, CPA proposed by Lee *et al.* [4] and MXPA developed by Xu-Jin [7], An *et al.* [8], Yamaguchi *et al.* [10], and Chen *et al.* [11] can be unified as EDA.

C. Comparison of Deorientation Algorithms

As aforementioned, $E = 0$ is the common requirement of CPA, MXPA, and VEDA. The correction process in MXPA of Xu-Jin and An is dedicated to extend the POA range according to the sign of $\tilde{C}$, and this idea is also adopted by VEDA. Nevertheless, VEDA uses $\tilde{C} \le 0$, taking the scattering mechanisms of the natural surface into consideration, while the correction in MXPA uses $\tilde{C} \ge 0$. Therefore, MXPA developed by Xu-Jin and An obtain different POA estimation from VEDA although the variation range is extended from 90° to 180°, as shown in Fig. 3(c) and (d), where the blue broken line denotes the real POA computed from DEM data by (7). Red solid line and green dotted line in Fig. 3(c) denote the results with and without range extension, respectively. φ_m is wrapped and only overlaps with the DEM-derived POA φ_{DEM} when $\varphi_{\mathrm{DEM}} \ge 0$ without extension. However, φ_{XJ} is totally deviated from φ_{DEM} after the range scope of POA is corrected because their definitions of the POA rotation direction and stipulations of the dominated co-pol power are different. Fig. 3(d) depicts φ_A in (21) with solid red line, which shows another kind of wrapping comparing to φ_{DEM}. Note that φ_A and φ_{XJ} are equal in their common range and both have 90° shift from φ_{DEM}. This is reasonable since range scope is the only difference between the two and they both select the h-pol power as dominated, which is different from φ_{DEM}.

TABLE I
COMPARISON OF DIFFERENT POA ESTIMATION ALGORITHMS

Symbol	Quantity	Range Value	Dominated Power
φ_{DEM}	DEM-derived	$[-90°, 90°]$	$\lvert\tilde{S}_{VV}\rvert^2$
φ	VEDA	$(-90°, 90°]$	$\lvert\tilde{S}_{VV}\rvert^2$
φ_L	CPA by Lee	$[-45°, 45°]$	undetermined
φ_C	MXPA by Chen		
φ_{XJ}	MXPA by Xu-Jin	$[0°, 180°)$	$\lvert\tilde{S}_{HH}\rvert^2$
φ_A	MXPA by An	$(-90°, 90°]$	$\lvert\tilde{S}_{HH}\rvert^2$
φ_Y	MXPA by Yamaguchi	$[-22.5°, 22.5°]$	undetermined

POA φ_C proposed by Chen *et al.* in (25) is the same as CPA-derived α in (18). As shown in Fig. 3(a), φ_C and α in solid red line are both limited in $[-45°, 45°]$, since both CPA and MXPA of Chen *et al.* have no additional constraint for further selecting POA from the two solutions of (8). When φ_{DEM} in blue broken line is in the range of $[-45°, 45°]$, φ_C and α are consistent with φ_{DEM}. Otherwise, they are wrapped into the limited range, and inaccurate estimation is then inevitable. Fig. 3(e) plots φ_Y developed by MXPA of Yamaguchi *et al.* [10], which further restricts POA in $[-22.5°, 22.5°]$ due to the use of the first-order derivative condition only. Thus, target deoriented by φ_Y not only has no fixed sign of $\tilde{C}$, but also cannot guarantee a reduction of its x-pol power. The range value and specified dominated co-pol power of each POA estimation algorithm are summarized in Table I, which enumerates their similarities and differences clearly.

V. EXPERIMENTAL RESULTS

A. Experiment on Simulated Mount Fuji Data

The ALOS PALSAR sample simulated data of Mount Fuji is utilized in this part to illustrate the efficacy of VEDA. Fig. 4(a) shows the Pauli image. The radar platform was moving from the left to the right of the image and was looking toward its right, i.e., the ground range direction is from the top to the bottom. The original single-look complex scattering matrix data is averaged in both azimuth and slant-range directions using a 2×10 boxcar filter to reduce the speckle noise and to make the multi-look pixel nearly square in pixel spacing. The aerial view of the same area from Google earth is shown in Fig. 4(b), and Fig. 4(c) displays the DEM data acquired by Shuttle Radar Topography Mission (SRTM) at a resolution

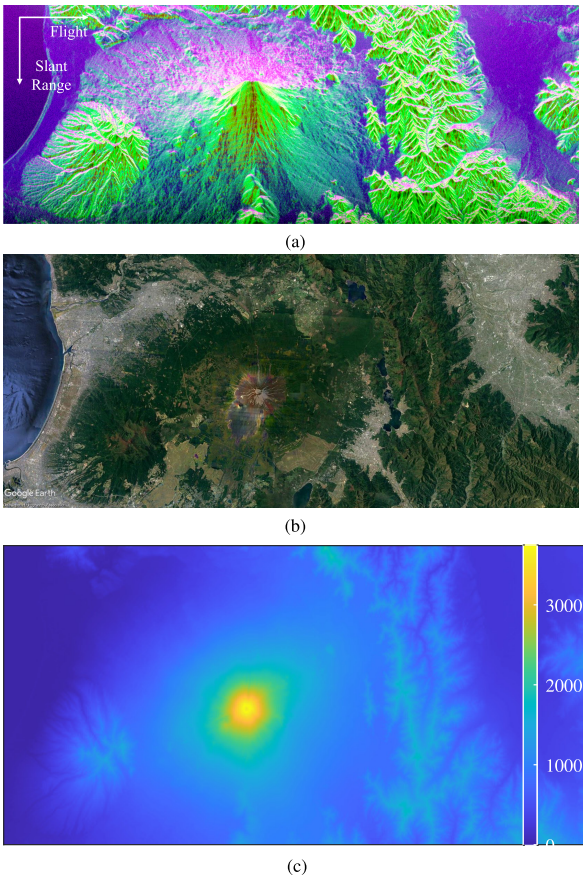

Fig. 4. Multi-source images of Mount Fuji in Japan used in the experiment. (a) Pauli RGB image of the sample PolSAR data from ALOS PALSAR. (b) Image of corresponding area from Google earth. (c) DEM image of corresponding area from SRTM.

of 1 arc-second (30 m). The leftmost area in the image is the Suruga Bay. A singular mountain lies to the left of Mount Fuji, which is the highest mountain in the center of the image, and its right is a mountain range. The rest area is flat ground, which can also be recognized from DEM data. Since PolSAR data is imaged in slant range while Google earth image and DEM data are formed based on ground range, differences among the images are caused. Besides, Fig. 4(a) shows severe perspective shrinkage in the main peak area due to the radar imaging geometry which seems totally different from Fig. 4(b) and (c).

Fig. 5(a) shows the orientation angle φ_{DEM} derived by (7) from DEM data, indicating the dramatic mountainous terrain fluctuation with large POA. From the color-bar we can see that the most of $|\varphi_{\mathrm{DEM}}|$ are greater than 45°. Fig. 5(b) shows the estimated POA φ by VEDA with (12). It can be observed that except for the different angles of view, φ and φ_{DEM} are highly consistent. POA φ of ocean and flat ground in Fig. 5(b) approaches 0, which is the same as φ_{DEM} in Fig. 5(a). The left side and the right side of a mountain possess POA of opposite signs in both images, which further brings Fig. 5(a) and (b) the tidy POA distribution, and we will analyze this in detail later.

POA α estimated by CPA is displayed in Fig. 5(c), which shows a chaotic and disordered orientation angle distribution. Since some of $|\varphi_{\mathrm{DEM}}|$ in this precipitously mountainous scene

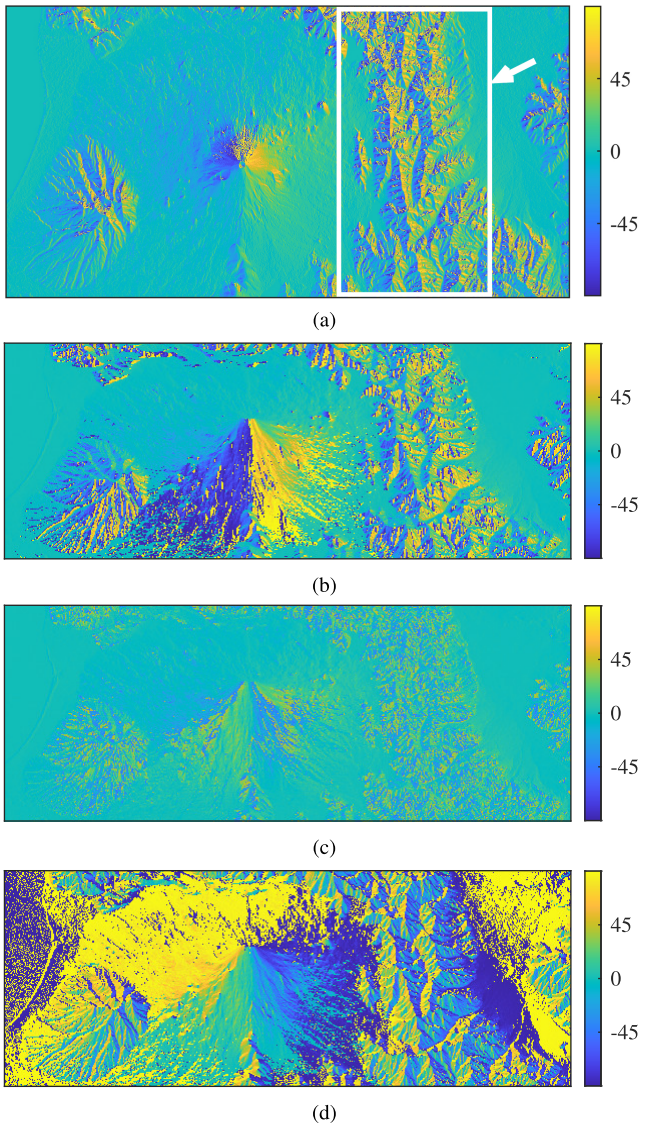

Fig. 5. POA estimation results achieved by (a) DEM based on geometrical relationship, (b) VEDA, (c) CPA, and (d) MXPA proposed by An [9] with angle unwrapping processing.

are larger than 45°, exceeding the limited range of α, large angle will be wrapped as a result. Hence the distribution of α will no longer take the middle of the mountain as a boundary, i.e., α cannot reflect the real terrain situation in Mount Fuji, despite the flat areas such as ocean and flat land have no wrapping in Fig. 5(c).

Fig. 5(d) shows An-derived POA φ_A with unwrapping operation, which extends the range of angle to $(-90°, 90°]$ [9]. However, φ_A looks strongly inconsistent with φ_{DEM}. For ocean area in the left side and some flat terrains between mountains, φ_A is about $\pm 90°$ alternatively in Fig. 5(d), instead of the real condition of 0° in Fig. 5(a). This is because φ_A is derived based on the assumption of h-pol power dominated, which will induce bias for the v-pol power dominated targets such as ocean and natural terrain modeled by Bragg scattering. Nevertheless, except for the 90° offset, the POA information in Fig. 5(d) and (b) is equivalent essentially. The POA estimated by Yamaguchi *et al.* [10] has been corrected by Chen *et al.* [11] which has the same expression

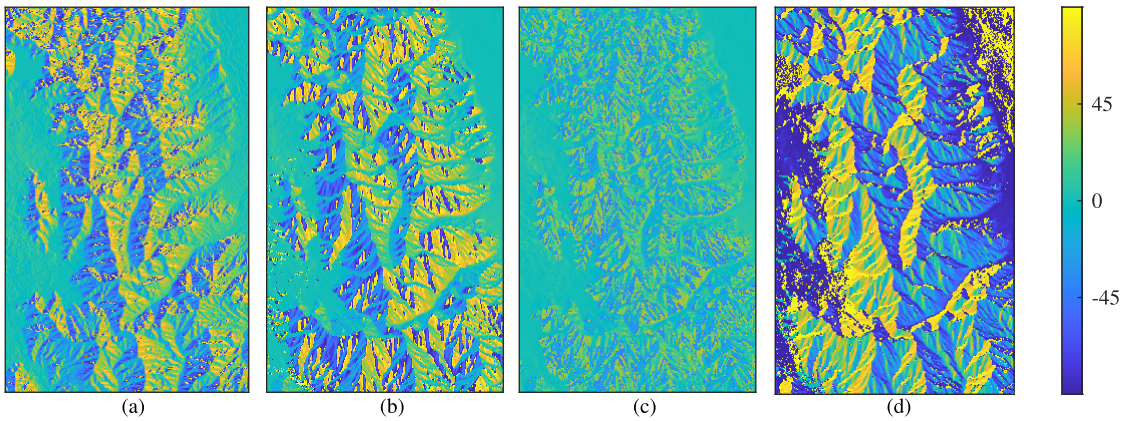

Fig. 6. Comparison of the POA estimations in steep mountain area obtained by (a) DEM based on geometrical relationship, (b) VEDA, (c) CPA, and (d) MXPA proposed by An [9] with angle unwrapping processing.

as CPA-derived POA and is represented in Fig. 5(c) also. Here, the result of MXPA by Xu and Jin is not demonstrated, because the algorithm is derived based on the Pauli vector $\boldsymbol{k}$ of a single target, instead of the coherency matrix $[T]$ of distribute target [7]. Besides, the range of φ_{XJ} is quite different from others and is hard to compare under the same color-bar system. Thus, we will not show them in the following experiments as well.

Fig. 6 further displays the POA estimations of the right mountain range, as framed by the white square in Fig. 5(a). The reason why POA of the left side of the mountain is opposite to that of the right side in Fig. 6(a) and (b) can be explained through analyzing the geometrical relationship of the two sides. Since the illumination direction is from the top to the bottom, the left and right sides of mountain have opposite azimuth slope angles, i.e., the left with negative azimuth angles while the right with positive ones. Fig. 2 shows that if two surface patches have the same ground range slopes but opposite azimuth slopes, their POA will be opposite to each other irrespective of whether the data is formatted in slant range or not. Such opposite POA in fact holds in all the mountain areas in Fig. 5(a) and (b).

Although the nice consistence, the slant-range φ cannot be exactly the same as the ground-range φ_{DEM} in each image pixel just due to the difference on viewpoint. It can be observed from both Figs. 5(b) and 6(b) that the sight-toward side of mountains, what we call sunny side, is compressed, while the opposite side, i.e., the nightside, is stretched severely in the PolSAR data because of the foreshortening effect of SAR imaging. Consequently, PolSAR-derived POA sketches more details than DEM-derived POA at nightside but misses some information on sunny side. Such a slant-range point of view makes Figs. 5(b) and 6(b) more stereo than the counterparts in Figs. 5(a) and 6(a). Note that POA of the nightside in Fig. 6(b) is slightly different from that in Fig. 6(a), but the difference is obvious for the 3776-m-high main peak of Mount Fuji between Fig. 5(a) and (b). This is also because of their different viewpoints primarily. Since PolSAR data is imaged in slant range, its relative topography will be different from the ground range data. And the difference will be more obvious for areas with more severe perspective shrinkage, e.g., the main peak. Hence, the nightside of the mountain shows a clearer positive–negative POA boundary in the middle of image than the DEM-derived result, even though they both present the phenomenon that the left and right sides of mountain have opposite POA. Besides, the process for SRTM data may also influence the accuracy of φ_{DEM} since interpolation is used after registering the DEM data to the same direction with PolSAR data.

In addition, since the data used in this subsection is the sample simulated data of ALOS PALSAR, even though it has been applied by some other researchers [22], another measured PolSAR data is employed to further substantiate the proposal.

B. Experiment on AIRSAR Data of Chiang Mai

Another interesting experiment is conducted on the real measured P-band PolSAR data of Chiang Mai, Thailand, from NASA/JPL TOPSAR. Fig. 7(a) shows its optical image from Google earth, as well as the flight and illumination directions of the radar. The illuminated mountainous ground is covered with vegetation, crops, and some village areas. NASA/JPL TOPSAR also acquired the corresponding DEM using C-band interferometric SAR, and the DEM-derived POA φ_{DEM} is shown in Fig. 7(b). It can be seen that φ_{DEM} is within $[-90°, 90°]$ and a nonnegligible amount of them are beyond $[-45°, 45°]$ (about 7% statistically). The CPA-derived POA α given in Fig. 7(c) shows apparent inconformity with DEM-derived result because of the narrow range. Fig. 7(d) shows POA φ estimated by VEDA, which is somewhat noisier than the DEM result, but the terrain profile and the POA distribution are highly consistent with Fig. 7(b). Fig. 7(e) is the filtered φ with 7×7 boxcar filter which seems less noisy than its original and it will be discussed in detail later. The PolSAR data has been filtered using a 5×5 boxcar filter to reduce the speckle effect.

It is noticeable that POA achieved by both CPA and VEDA are unclear and noisy in Fig. 7(c)–(e). In addition to the influence of vegetation on the ground, the low resolution and speckle of P-band PolSAR data may also contribute to the imperfection. As a result, many minuscule slope variations drowning in the noise cannot be identified, which leads to the

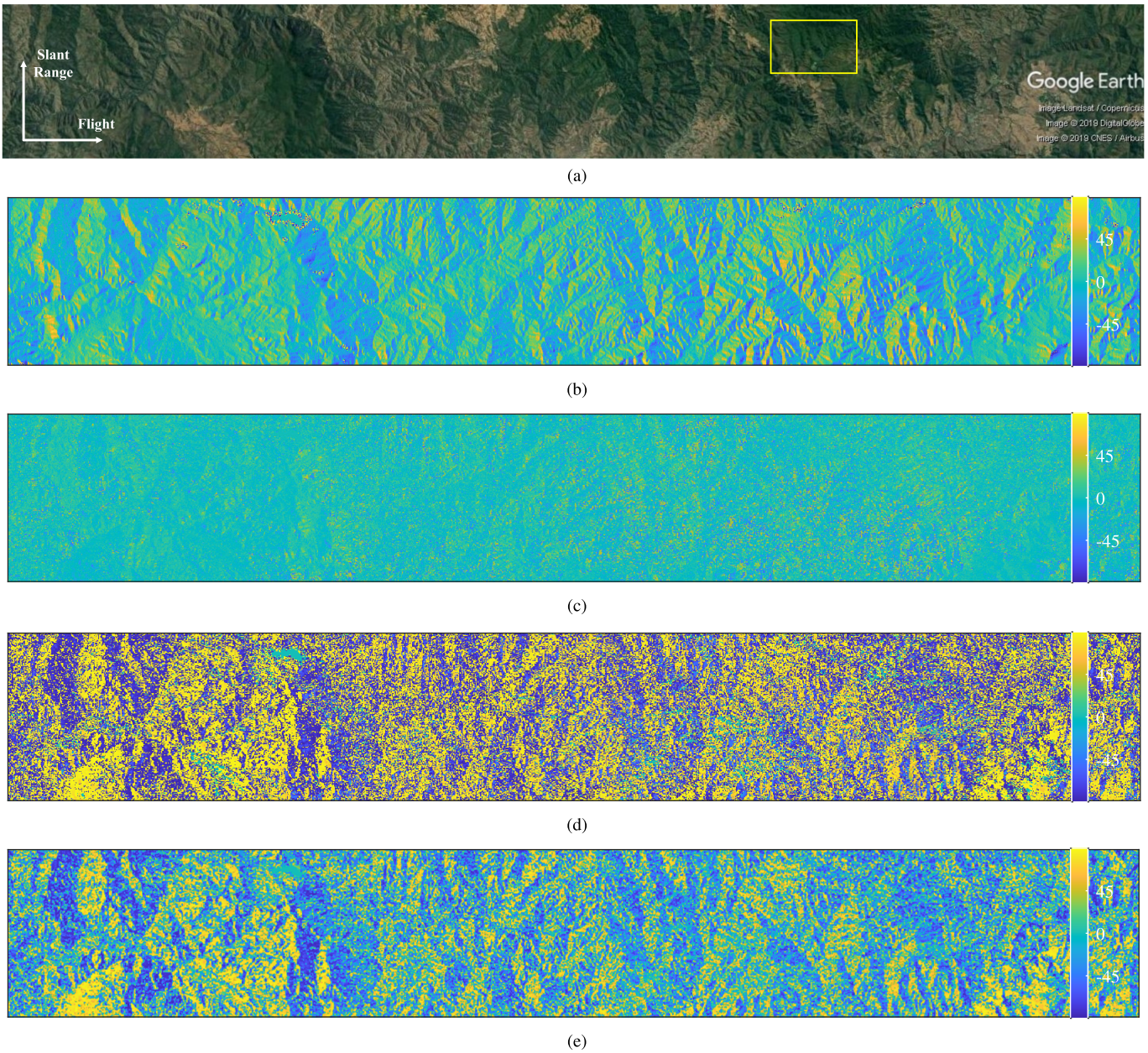

Fig. 7. Images of experimental area in Chiang Mai, Thailand. (a) Optical image from Google earth. POA estimation results obtained by (b) DEM based on geometrical relationship, (c) CPA, and VEDA (d) without and (e) with POA filtering operation, respectively. The PolSAR data has been filtered using a 5×5 boxcar filter to reduce the speckle effect, and (e) is the filtered result of (d) by a 7×7 boxcar filter.

vague estimation results. Nevertheless, the better performance of VEDA can still be observed.

For a detailed comparison, we focus on a small area with size 140×300, as circumscribed by the yellow square in Fig. 7(a). It can be seen from Fig. 8(a), (b), and (d) that even though the ground is mantled by trees, VEDA is effective in POA estimation, while the result of CPA, in Fig. 8(c), can hardly reflect the topographic information. Furthermore, Fig. 9 exhibits a quantitative comparison of estimated POA for a 300-pixel cut in azimuth direction of Fig. 8 (i.e., the red line). Three profiles of estimated POA derived by DEM, CPA, and VEDA are given, respectively. It can be seen that VEDA-derived POA φ matches φ_{DEM} in general, though with certain fluctuations at some special points, which can be attributed to the land vegetation on the ground and the reason will be analyzed later. CPA-derived POA shows an inferior result which seems uncorrelated with φ_{DEM}. Considering many φ_{DEM} are fluctuating around $\pm 45°$, this may be because of its limited range. The scatter diagrams of φ_{DEM} versus α and φ are given in Fig. 10(a) and (b), respectively, where blue dashed lines show the theoretical results of the two algorithms, and the theoretical wrapped POA achieved by CPA can be seen clearly in Fig. 10(a). Though there are several unideal biased points in the plot Fig. 10(b), φ is accordance with the theoretical values. The unideal performance of α may due to the joint effect of noise and phase wrapping. Take φ_{DEM} as the reference, we compute the mean and root mean square (rms) of the differences, as well as the Pearson product-moment correlation coefficient (PPMCC, which ranges from -1 to 1) between α and φ_{DEM} and that between φ and φ_{DEM}.

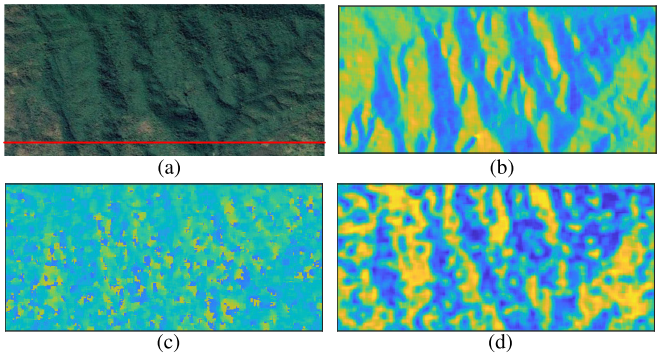

Fig. 8. Detailed analysis of the experimental data on a 140×300 area, with (a) optical image and derived POA by (b) DEM, (c) CPA, and (d) VEDA.

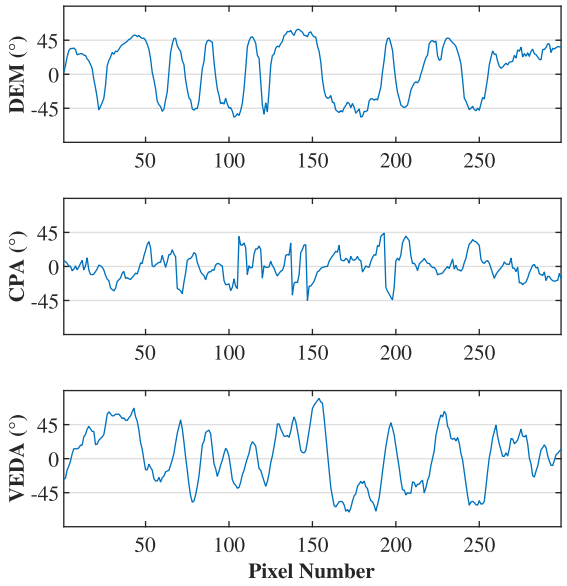

Fig. 9. Comparison of DEM-derived POA, CPA-derived POA, and VEDA-derived POA of the azimuth range cut samples shown in Fig. 8(a). Result of VEDA is more accordance with the result of DEM.

As listed in Table II, CPA holds large mean, large rms difference, and negative PPMCC, i.e., 40.43°, 45.43°, and −0.37, because of the range limitation, while VEDA shows better performance as the mean difference is 21.84°, rms difference is 26.92°, and PPMCC is 0.73. It can be derived that the theoretical value of PPMCC between φ and φ_{DEM}, and α and φ_{DEM} is 1 and −0.25, respectively, where the negative sign of the latter is ascribed to the phase wrapping. Actually, the quantitative result of VEDA is barely satisfactory, about which will be analyzed in the following.

It should be noted that a 7×7 boxcar filter is imposed only on the VEDA-derived POA φ in this detailed comparing experiment, i.e., Figs. 8–10, and Table II all display the results of filtered φ and unfiltered CPA-derived POA α. There are two important reasons for this. First, no filtering on α is not only because of the following to Lee *et al.* [4]–[6], [16], but also because of its range restriction. In this experiment, many φ_{DEM} are fluctuating around ±45°. After filtering, some φ_{DEM} exceeding $[-45°, 45°]$ are smoothed and move into $[-45°, 45°]$. For instance, if 5 contiguous φ_{DEM} distribute as

$$40° \quad 47° \quad 43° \quad 46° \quad 45°$$

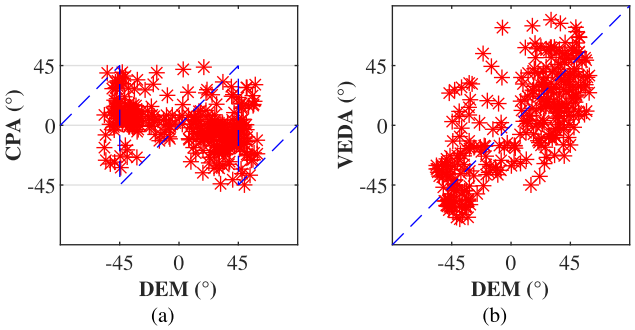

Fig. 10. Scatter diagrams comparing DEM-derived POA with (a) CPA-derived POA and (b) VEDA-derived POA. The dashed blue lines represent the theoretical values of CPA-derived POA and VEDA-derived POA, respectively.

TABLE II
STATISTICAL DIFFERENCES BETWEEN DEM-DERIVED POA AND POLSAR-DERIVED POA

Algorithms	Mean of Difference	RMS of Difference	PPMCC
CPA	40.43°	45.43°	−0.37
VEDA	21.84°	26.92°	0.73

after filtering by an average filter of length 2, it becomes

$$43.5° \quad 45° \quad 44.5° \quad 45.5° \quad 45°.$$

However, because of the limited range, CPA-derived POA α exceeding $[-45°, 45°]$ are wrapped before filtering, which will change the angular sign, as (ideally)

$$40° \quad -43° \quad 43° \quad -44° \quad 45°.$$

Then, the filtered result is

$$-1.5° \quad 0° \quad -0.5° \quad 0.5° \quad 45°$$

which holds a large difference with φ_{DEM}. It is worth mentioning that we have experimented a lot about filtering on α (not only in this scene), and the results show that it cannot increase the CPA accuracy, and only lead to over-smoothing. Therefore, it is rational to leave the CPA-derived POA unfiltered as done by the previous work [4]–[6], [16]. Second, compared with CPA and other estimation algorithms which limit the POA range in $[-45°, 45°]$, VEDA is somewhat more susceptible to the noise, because it strongly relies on the relative value of $|S_{VV}|$ and $|S_{HH}|$. Even slight fluctuation of the co-pol powers may change the result of VEDA. As can be seen in Fig. 7(d), which shows unfiltered VEDA-derived POA φ, even though it is consistent with the general profile of φ_{DEM} visually, the noise spots in the figure are non-negligible, and the value of POA fluctuates around ±90° severely, which greatly reduces the feasibility for further quantitative analysis. In contrast, the filtering result shown in Fig. 7(e) significantly suppresses the noise. Thus, it is necessary to filter the result of VEDA for reducing the influence of random noise. Here we employ the 7×7 boxcar filter on φ, which is a nice compromise between the image resolution and noise level. Even so, the undesired fluctuations still greatly decrease the accuracy of VEDA, as aforementioned. Undoubtedly, the stronger the

imposed filter is, the less the number of the outlier points (as can be seen in Fig. 10(b)) will be, nevertheless, the estimated POA will also be over-smoothing meanwhile. Accordingly, there needs to be more efforts to investigate the relationship between random noise suppression and detail preserving of the POA estimation in the future work.

The influence of vegetation and village areas on POA estimation is discussed as follows. POA results of these areas are inconsistent with φ_{DEM}, and this is because of the inconformity of the scattering models. As aforementioned, VEDA is proposed for terrain POA estimation, and it relies on the relative value between $|S_{HH}|^2$ and $|S_{VV}|^2$. Since both vegetation areas dominated by volume scattering and village areas dominated by double-bounce scattering dissatisfy the hypothesis, the result of VEDA will be inaccurate. Therefore, VEDA should be employed on suitable scenes, i.e., for terrain surface. On the other hand, this also implies that the scattering characteristic-dependent algorithm VEDA may differentiate the natural surface and other scattering type effectively, which may be employed in terrain classification in the future work.

VI. Conclusion

This article presents a novel POA estimation algorithm VEDA for terrain slope estimation on the basis of the natural surface scattering characteristics, which extends the range of POA to the unwrapped range calculated by DEM data. The ALOS PALSAR sample data of Mount Fuji and AIRSAR data of Chiang Mai substantiate the algorithm well. The influence and necessity of filtering on estimated POA are also discussed in the experiments. Due to the influence of volume scattering from vegetation and the different polarization characteristics of the villages, some unexpected noises are also shown in the results, which needs further investigation to resolve. In conclusion, for bare and less vegetation surface, VEDA can estimate POA accurately without angle wrapping and ambiguity.

Current deorientation algorithms are analyzed and compared with VEDA in the article for investigating the essential relationship among them. By deriving the alternative solution of CPA, we provide the proof that CPA and MXPA are equivalent. Besides, their differences in angle definition and range limitation are discussed in detail, which clarifies the wrapping and unwrapping mechanisms of POA. Since all of them take Huynen parameter E as zero when target has no orientation, they can be collectively called EDA.

Appendix A

This appendix presents the two solutions of (8) in Section III-A and proves one of it is the solution of VEDA, i.e., it satisfies (10) and (11) in Section III-B.

According to (8) and (9), the solution of EDA in $[-45^\circ, 45^\circ]$ is

$$\begin{cases} \sin 4\theta_1 = \dfrac{E}{\sqrt{E^2+B^2}} \\ \cos 4\theta_1 = \dfrac{B}{\sqrt{E^2+B^2}} \end{cases}, \quad \theta_1 \in [-45^\circ, 45^\circ]. \tag{A.1}$$

Since the range of POA is $[-90^\circ, 90^\circ]$, we can derive the other solution as

$$\theta_2 = \begin{cases} \theta_1 + 90^\circ, & -45^\circ \le \theta_1 \le 0^\circ \\ \theta_1 - 90^\circ, & 0^\circ < \theta_1 \le 45^\circ \end{cases} \tag{A.2}$$

where θ_2 not only ranges in $[-90^\circ, 90^\circ]$, but also satisfies (8) and (9). Therefore, θ_1 and θ_2 are the two solutions of (8).

According to (11), the deoriented Huynen parameter $\tilde{C}$ by utilizing the two solutions of (8) can be expressed respectively as

$$\begin{cases} \tilde{C}_1 = C\cos 2\theta_1 + H\sin 2\theta_1 \\ \tilde{C}_2 = C\cos 2\theta_2 + H\sin 2\theta_2 \,. \end{cases} \tag{A.3}$$

Substituting (A.2) into (A.3), we have

$$\begin{aligned} \tilde{C}_2 &= C\cos(2\theta_1 \pm 180^\circ) + H\sin\left(2\theta_1 \pm 180^\circ\right) \\ &= -C\cos 2\theta_1 - H\sin 2\theta_1 \\ &= -\tilde{C}_1. \end{aligned} \tag{A.4}$$

Therefore, $\tilde{C}_1$ and $\tilde{C}_2$ have opposite signs, which indicates that one of the solutions of (8) always satisfies (10) and (11).

Appendix B

This appendix is devoted to deriving $\alpha = \varphi_L$ mentioned in Section IV-A. Let

$$\tan^{-1}\frac{-E}{-B} = 4\theta \tag{B.1}$$

which means that

$$\begin{cases} \sin 4\theta = \dfrac{-E}{\sqrt{E^2+B^2}} \\ \cos 4\theta = \dfrac{-B}{\sqrt{E^2+B^2}} \end{cases}, \quad \theta \in \left[-45^\circ, 45^\circ\right]. \tag{B.2}$$

Then, (15) can be expressed by θ as

$$\varphi_L = \begin{cases} \theta + 45^\circ, & \theta \le 0 \\ \theta - 45^\circ, & \theta > 0 \,. \end{cases} \tag{B.3}$$

On the other hand, based on the property of trigonometric function,

$$\tan^{-1}\frac{E}{B} = \tan^{-1}\frac{-E}{-B} \pm 180^\circ \tag{B.4}$$

thus (18) can be rewritten as

$$\alpha = \theta \pm 45^\circ. \tag{B.5}$$

Since the range of α should be limited in $[-45^\circ, 45^\circ]$, it becomes

$$\alpha = \begin{cases} \theta + 45^\circ, & \theta \le 0 \\ \theta - 45^\circ, & \theta > 0 \end{cases} \tag{B.6}$$

which is the same as (B.3).

Theoretically, there is a one-to-one correspondence between the calculated POA and the real orientation angle. But a bias may exist because of the periodicity property of the trigonometric function. Essentially, this involves in how to define the zero-orientation direction of a target, which will affect the value of POA. The two solutions of (17) represent two opposite zero-orientation directions. The procedure of

removing bias by adding 180° as Lee *et al.* did just changes the direction from one solution to another, which matches the data characteristics better. That is the essential reason why α and φ_L have the same expression.

APPENDIX C

Here, we solve (22) and (24) to formulate an explicit expression of (25) given by Chen *et al.* in the range of $[-45°, 45°]$ and to prove $\alpha = \varphi_C$.

Equations (22) and (24) can be simplified as

$$B \sin 4\varphi_C - E \cos 4\varphi_C = 0 \tag{C.1}$$

$$B \cos 4\varphi_C + E \sin 4\varphi_C > 0\,. \tag{C.2}$$

From the previous discussion we know that if the sign of $\sin 4\varphi$ and $\cos 4\varphi$ are given, the range of φ can be extended to $[-45°, 45°]$. Therefore, the second order deviation condition is indispensable. From (C.1), E can be represented by

$$E = B\frac{\sin 4\varphi_C}{\cos 4\varphi_C}. \tag{C.3}$$

Substituting (C.3) into (C.2), we have

$$B \cos 4\varphi_C + B\frac{\sin^2 4\varphi_C}{\cos 4\varphi_C} > 0 \quad \Rightarrow \quad \frac{B}{\cos 4\varphi_C} > 0 \tag{C.4}$$

which means B and $\cos 4\varphi_C$ are of the same sign. Similarly, it is easy to derive that E and $\sin 4\varphi_C$ are of the same sign. Therefore, φ_C can be derived in the range of $[-45°, 45°]$ by

$$\begin{cases} \sin 4\varphi_C = \dfrac{E}{\sqrt{E^2 + B^2}} \\ \cos 4\varphi_C = \dfrac{B}{\sqrt{E^2 + B^2}} \end{cases} \tag{C.5}$$

which is equivalent to the expression of α. Hence, the POA result of the MXPA proposed by Chen *et al.* is the same as CPA developed by Lee *et al.*.

ACKNOWLEDGMENT

The authors would like to thank the Japan Aerospace Exploration Agency (JAXA) and the National Aeronautics and Space Administration's Jet Propulsion Laboratory (NASA/JPL) for providing the outstanding ALOS-PALSAR and AIRSAR polarimetric SAR data, respectively. The authors would also like to thank the anonymous reviewers for their pertinent comments and constructive suggestions in making this article a better presentation.

REFERENCES

[1] J. R. Huynen, "Phenomenological theory of radar targets," Ph.D. dissertation, Dept. Elect. Eng., Math. Comput. Sci., Tech. Univ. Delft, Delft, The Netherlands, 1970.

[2] J.-S. Lee and E. Pottier, *Polarimetric Radar Imaging: From Basics to Applications*. Boca Raton, FL, USA: CRC Press, 2009.

[3] D. L. Schuler, J.-S. Lee, and G. De Grandi, "Measurement of topography using polarimetric SAR images," *IEEE Trans. Geosci. Remote Sens.*, vol. 34, no. 5, pp. 1266–1277, Sep. 1996.

[4] J.-S. Lee, D. L. Schuler, and T. L. Ainsworth, "Polarimetric SAR data compensation for terrain azimuth slope variation," *IEEE Trans. Geosci. Remote Sens.*, vol. 38, no. 5, pp. 2153–2163, Sep. 2000.

[5] J.-S. Lee, D. L. Schuler, T. L. Ainsworth, E. Krogager, D. Kasilingam, and W.-M. Boerner, "On the estimation of radar polarization orientation shifts induced by terrain slopes," *IEEE Trans. Geosci. Remote Sens.*, vol. 40, no. 1, pp. 30–41, Jan. 2002.

[6] J.-S. Lee and T. L. Ainsworth, "The effect of orientation angle compensation on coherency matrix and polarimetric target decompositions," *IEEE Trans. Geosci. Remote Sens.*, vol. 49, no. 1, pp. 53–64, Jan. 2011.

[7] F. Xu and Y.-Q. Jin, "Deorientation theory of polarimetric scattering targets and application to terrain surface classification," *IEEE Trans. Geosci. Remote Sens.*, vol. 43, no. 10, pp. 2351–2364, Oct. 2005.

[8] W. An, Y. Cui, and J. Yang, "Three-component model-based decomposition for polarimetric SAR data," *IEEE Trans. Geosci. Remote Sens.*, vol. 48, no. 6, pp. 2732–2739, Jun. 2010.

[9] W. An, "The polarimetric decomposition and scattering characteristic extraction of polarimetric SAR," Ph.D. dissertation, Dept. Inf. Commun. Eng., Tsinghua Univ., Beijing, China, 2010.

[10] Y. Yamaguchi, A. Sato, W.-M. Boerner, R. Sato, and H. Yamada, "Four-component scattering power decomposition with rotation of coherency matrix," *IEEE Trans. Geosci. Remote Sens.*, vol. 49, no. 6, pp. 2251–2258, Jun. 2011.

[11] S.-W. Chen, M. Ohki, M. Shimada, and M. Sato, "Deorientation effect investigation for model-based decomposition over oriented built-up areas," *IEEE Geosci. Remote Sens. Lett.*, vol. 10, no. 2, pp. 273–277, Mar. 2013.

[12] F. Y. Zhu, Y. H. Zhang, and D. Li, "A novel deorientation method in PolSAR data processing," *Remote Sens. Lett.*, vol. 7, no. 11, pp. 1083–1092, Aug. 2016.

[13] O. Antropov, Y. Rauste, H. Astola, J. Praks, T. Hame, and M. T. Hallikainen, "Land cover and soil type mapping from space-borne PolSAR data at L-band with probabilistic neural network," *IEEE Trans. Geosci. Remote Sens.*, vol. 52, no. 9, pp. 5256–5270, Sep. 2014.

[14] S.-W. Chen, X.-S. Wang, S.-P. Xiao, and M. Sato, "General polarimetric model-based decomposition for coherency matrix," *IEEE Trans. Geosci. Remote Sens.*, vol. 52, no. 3, pp. 1843–1855, Mar. 2014.

[15] D. Li and Y. Zhang, "Adaptive model-based classification of Pol-SAR data," *IEEE Trans. Geosci. Remote Sens.*, vol. 56, no. 12, pp. 6940–6955, Dec. 2018.

[16] J.-S. Lee, T. L. Ainsworth, and Y. Wang, "Polarization orientation angle and polarimetric SAR scattering characteristics of steep terrain," *IEEE Trans. Geosci. Remote Sens.*, vol. 56, no. 12, pp. 7272–7281, Dec. 2018.

[17] S. R. Cloude, *Polarisation: Applications in Remote Sensing*. Oxford, U.K.: Oxford Univ. Press, 2010.

[18] I. Hajnsek, E. Pottier, and S. R. Cloude, "Inversion of surface parameters from polarimetric SAR," *IEEE Trans. Geosci. Remote Sens.*, vol. 41, no. 4, pp. 727–744, Apr. 2003.

[19] S. R. Cloude and E. Pottier, "A review of target decomposition theorems in radar polarimetry," *IEEE Trans. Geosci. Remote Sens.*, vol. 34, no. 2, pp. 498–518, Mar. 1996.

[20] J. R. Huynen, "Extraction of target significant parameter from polarimetric data," P.Q. Res., Los Altos Hills, CA, USA, Tech. Rep. 103, 1988.

[21] D. Li and Y. Zhang, "Unified huynen phenomenological decomposition of radar targets and its classification applications," *IEEE Trans. Geosci. Remote Sens.*, vol. 54, no. 2, pp. 723–743, Feb. 2016.

[22] S. Kusano, M. Watanabe, and M. Sato, "Proposal of a new algorithm of the three-component decomposition for azimuthally inclined objects," JAXA Special Publication, ALOS Res. Anouncement Programs 1&2, Final Rep. JAXA-SP-11-007E, 2011.

Liting Liang (Graduate Student Member, IEEE) received the B.S. degree in electronic information engineering from Harbin Engineering University, Harbin, China, in 2016. She is pursuing the Ph.D. degree in electromagnetic and microwave technology in the National Space Science Center, Chinese Academy of Sciences, Beijing, China.

Her research interest includes polarimetric synthetic aperture radar image processing and classification.

Yunhua Zhang (Member, IEEE) received the B.S. degree in electrical engineering from Xidian University, Xi'an, China, in 1989 and the M.S. and Ph.D. degrees in electrical engineering from Zhejiang University, Hangzhou, China, in 1993 and 1995, respectively.

He is a Professor with the National Space Science Center, Chinese Academy of Sciences, Beijing, China, and the Director of the CAS Key Laboratory of Microwave Remote Sensing. He is also a Professor with the School of Electronic, Electrical, and Communication Engineering, University of Chinese Academy of Sciences, Beijing, where he lectured the modern radar theory and technology to the postgraduate students. His research interests include the system design and signal processing of microwave sensors (high-resolution radar, interferometric radar, radar altimeter, and noise radar), polarimetric radar target decomposition, application of compressive sensing in radar, and antennas and computational electromagnetics.

Dr. Zhang is the Chief Designer for the Chinese Tiangong-2 Interferometric Imaging Altimeter, which is the first spaceborne wide-swath radar altimeter launched in September 15, 2016.

Dong Li (Member, IEEE) received the B.S. degree in electronic engineering from Xidian University, Xi'an, China, in 2008 and the Ph.D. degree in electrical engineering from the University of Chinese Academy of Sciences, Beijing, China, in 2013.

He is an Associate Professor with the CAS Key Laboratory of Microwave Remote Sensing, National Space Science Center, Chinese Academy of Sciences, Beijing. His research interests include synthetic aperture radar (SAR) polarimetry, polarimetric target decomposition, polarimetric scattering modeling, SAR image registration, and computer SAR vision.

Dr. Li was elected as a Member of the Youth Innovation Promotion Association, Chinese Academy of Sciences in 2014. He received the President Scholarship for Outstanding Students of Chinese Academy of Sciences in 2013 for his Ph.D. dissertation on the stereo processing and polarimetric analysis of SAR images.